nature physics

SUPPLEMENTARY INFORMATION

DOI: 10.1038/NPHYS3234

Dynamics and inertia of skyrmionic spin structures

Felix Büttner,[1,2,3,*] C. Moutafis,[4,†] M. Schneider,[3] B. Krüger,[1] C. M. Günther,[3] J. Geilhufe,[5] C. v. Korff Schmising,[3] J. Mohanty,[3,‡] B. Pfau,[3] S. Schaffert,[3] A. Bisig,[1] M. Foerster,[1] T. Schulz,[1] C. A. F. Vaz,[1,6] J. H. Franken,[7] H. J. M. Swagten,[7] M. Kläui,[1] and S. Eisebitt[3,5]

[1]*Institute of Physics, Johannes Gutenberg-Universität Mainz, Staudinger Weg 7, 55128 Mainz, Germany*

[2]*Graduate School Materials Science in Mainz, Staudinger Weg 9, 55128 Mainz, Germany*

[3]*Institut für Optik und Atomare Physik, Technische Universität Berlin, Straße des 17. Juni 135, 10623 Berlin, Germany*

[4]*Swiss Light Source, Paul Scherrer Institut, 5232 Villigen PSI, Switzerland*

[5]*Helmholtz-Zentrum Berlin für Materialien und Energie GmbH, Hahn-Meitner-Platz 1, 14109 Berlin, Germany*

[6]*SwissFEL, Paul Scherrer Institut, 5232 Villigen PSI, Switzerland*

[7]*Department of Applied Physics, Center for NanoMaterials, Eindhoven University of Technology, P.O. Box 513, 5600 MB Eindhoven, The Netherlands*

(Dated: December 10, 2014)

DOI: 10.1038/NPHYS3234

I. TOPOLOGICAL CONFINEMENT OF SKYRMIONS

The special topology defining all skyrmionic vector fields is characterized by the possibility to continuously deform their domain space to a spherical shape, while retaining their image (*homotopy* of the vector field to the identity map of the sphere, illustrated in Fig. 1 of the main text).[1] For integer Skyrmion number N, the boundary of the domain space is mapped to one of the poles of the sphere, and an area in the interior is mapped to the other pole. These two areas, called domains, are smoothly connected by a closed loop domain wall. Both the inner domain and the domain wall never touch any boundary of the domain space; they are confined in all dimensions by the outer domain. Most often, the combination of inner domain and domain wall exhibits particle-like properties, and the corresponding quasiparticles are called Skyrmions. We point out that the definition of Skyrmions is independent of the mechanisms leading to their physical stabilization. In particular, there are subtle differences between the spin structures of bubbles and chiral Skyrmions, which possibly lead to distinct physical properties.[2] The topological mass determined in this work, however, is associated with the finite extent of the Skyrmions, which is a common property of all Skyrmions.

II. THEORETICAL BACKGROUND

Here we show how our experimental results are embedded in a preexisting theoretical framework on Skyrmion gyrotropic motion, which we will shortly review. In particular, we will give a short summary of the key results of Refs. 2, 12, and 17 of the main paper.

Already in 1973, Thiele[3] derived from theoretical arguments that rigid bubbles experience a force perpendicular to their velocity. Later, Papanicolaou and Tomaras[4] provided an intuitive explanation of this phenomenon by showing that the Skyrmion number of a magnetic structure can be interpreted as an intrinsic angular momentum of the structure. The resulting equation of motion for the centre of the structure, the so-called Thiele equation, reads

$$\mathbf{G} \times \dot{\mathbf{R}} + D\dot{\mathbf{R}} - \partial_{\mathbf{R}} U = 0. \tag{1}$$

This equation has proven extremely useful and valid for the description of low frequency bubble dynamics as well as of low and high frequency vortex dynamics (vortices are structures with Skyrmion number

$N = \pm 1/2$). However, the equation has recently been challenged by micromagnetic simulations of bubble dynamics in the GHz regime.[5] In their theoretical study, Moutafis *et al.*[5] suggested that the detailed shape of the bubble motion is not a smooth spiral as predicted by Eq. (1), but rather a hypocycloid with five cusps per turn (as visible in Fig. 2b). A movie of this simulated irregular gyration is attached.

The surprising shape of the bubble trajectory could be explained in 2012 by Makhfudz *et al.*[6] by extending Eq. (1) by a second order temporal derivative of $\mathbf{R}$. As discussed in the chapter IX, the second order differential equation has two solutions, one describing a clockwise motion and one describing a counter-clockwise motion. If both frequencies are different in magnitude, and if the higher frequency mode (say, ω_h) has a smaller amplitude than the lower frequency mode (ω_l), then the superposition of both modes is a hypocycloid with $|\omega_h/\omega_l| + 1$ cusps per cycle.

As common in physics, the presence of a second order temporal derivative is associated with inertia, and the coefficient of this second order term is called "effective mass". To explain the source of this mass, the authors describe the motion of the bubble by suitable spin waves propagating along the domain wall (that separates the bubble interior from the environment). To realise such waves, the spins in the domain wall have to tilt within the plane of the magnetic film out of their equilibrium orientation (that is, tangential to the domain wall), which is energetically unfavourable because it creates magnetic volume charges (divergence of the magnetisation). The energy associated with such a tilt of the spins can be described by an effective anisotropy, the so-called transverse anisotropy. This phenomenon is generic for domain walls, straight or curved, and leads to inertia, as argued by Döring already in 1948.[7]

The theory by Makhfudz *et al.* thus predicts that the mass of the bubble is equivalent to the Döring mass of its domain wall. However, we find that the mass of the bubble is at least five times larger than this prediction. The discrepancy must be an additional source of inertia. In our model, this inertia comes from the possibility of the confined bubble to perform other collective excitations, such as the so called breathing. This breathing, which corresponds to an expansion and shrinking of the total areal extent of the bubble, is clearly visible in the attached movie of the simulated gyration. In this simulation, the breathing is synchronous to the cusps of the trajectory, supporting our claim of a relation between the inertia-induced cusps and the breathing of the bubble.

Recently, Mochizuki has suggested by simulations that chiral Skyrmions show the same characteristic gy-

DOI: 10.1038/NPHYS3234

ration at the GHz scale.[8] He has found a clockwise rotational mode ($\omega_{\mathrm{CW}} \approx 0.6\,\mathrm{GHz}$), a counter-clockwise rotational mode ($\omega_{\mathrm{CCW}} \approx 1.1\,\mathrm{GHz}$), and a breathing mode ($\omega_{\mathrm{BR}} \approx 0.8\,\mathrm{GHz}$). The presence of both chiral modes unambiguously points to the presence of inertia, and the given values are similar to our observations, corroborating our conclusion that the inertia reported by us is a common feature of all skyrmionic spin structures.

III. MOVIE OF THE BUBBLE DYNAMICS

In the following section, we present the complete set of dynamic magnetic images used to obtain the bubble trajectory presented in Fig. 2 of the main text. The images are sorted chronologically by their time delay. They are presented individually in Fig. 1 and in a compressed movie attached to this document. The time delay of each image is indicated by a coloured dot in the top-right of each image in Fig. 1 and by a sketch of the pulse shape in the top of each frame of the movie. The movie presents the images at a constant frame rate, i.e., the time between two images of the movie does not correspond to the time delay between these images. The images show a number of details beyond the motion of one of the bubbles discussed in the main text. These features are interesting by themselves, but not significant for the interpretation of the observed trajectory of the bubble, as we shall see next:

The most important observation is the presence of a second bubble in all frames of the movie. In contrast to the bubble that we discuss in the main paper, this bubble seems to be immune against the external excitation and against the stray field of the third domain. This behaviour can be explained by a particularly deep and steep local potential minimum in which the bubble is trapped. The tiny motion within such a potential is beyond our resolution. For the present case, since we are interested in the motion of an individual bubble, this pinning of the second bubble is actually highly desirable; without any significant dynamic changes, the interaction between the two bubbles is fully described by a static offset in the magnetostatic potential U. This means that the interaction between the two bubbles significantly alters the total potential of the moving bubble, but this total potential remains static and it can locally be approximated by a parabola. That is, in the laboratory frame, the moving bubble behaves effectively like an isolated magnetic Skyrmion. The stiffness of the local parabolic potential is a fitting parameter in our analysis, which means that we do not have to know

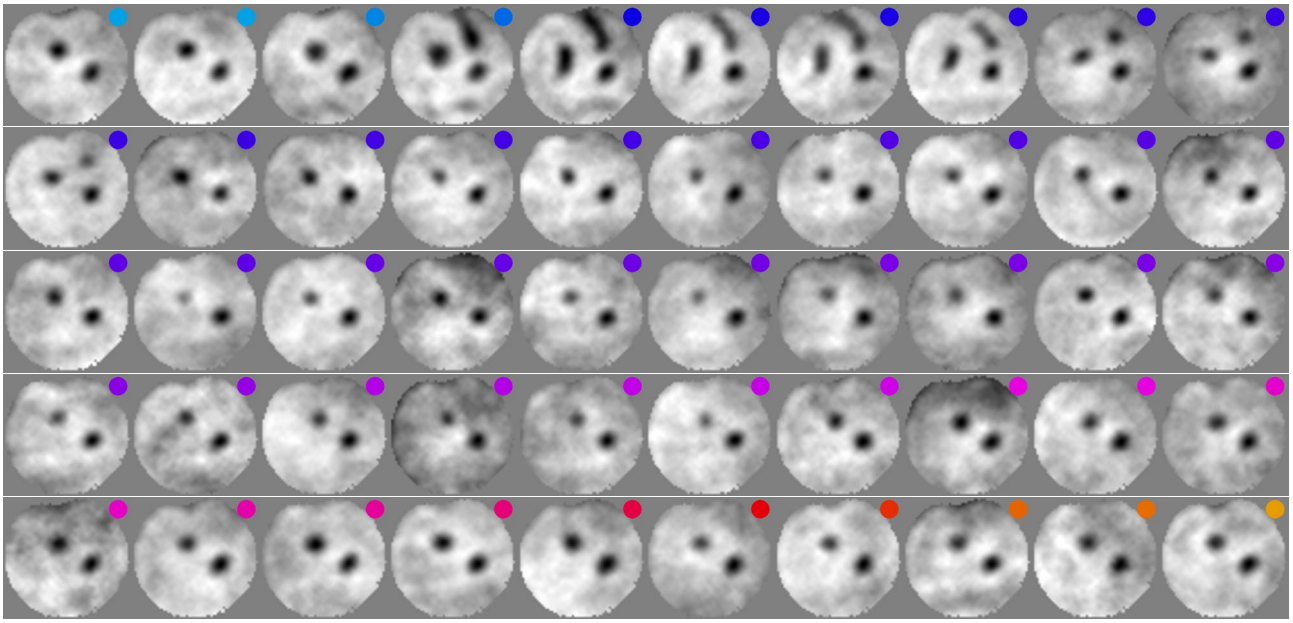

Figure 1 | Collection of all dynamic images acquired. The coloured dot in the top-right corner of each images indicates the time delay of the respective image, as defined in Fig. 2b of the main text.

the type or strength of the interaction between the two bubbles. We furthermore note that this situation of just one moving object is totally different from previous experiments on vortex pairs (e.g., Ref. 9), where both entities are moving in the laboratory frame. Another important distinction to the rotating vortex experiment is that bubbles, in contrast to vortices, interact only through stray fields; at the observed distances, the bubbles are not coupled by the magnetic exchange interaction. This is an inherent property of skyrmionic structures: as discussed in detail in section I, Skyrmions are localized objects. This means that two Skyrmions that do not touch each other cannot interact via a local coupling such as the exchange energy. Only the non-local dipolar coupling can mediate an interaction between Skyrmions (Skyrmions are thus asymptotically free). This is one of the properties that make these objects interesting for storage devices.

Another interesting observation is the change of shape and contrast of the tracked bubble. During the presence of the third domain, the tracked bubble elongates to a stripe-like shape, which can be viewed as an higher order excitation.[6] Such a behaviour during extreme excitation is not described well within the limitations of our point-like quasiparticle model of the Skyrmion motion underlying Eq. (1) of the main paper. A possible explanation for the asymmetric extension of the bubble is an anisotropic potential landscape, in

DOI: 10.1038/NPHYS3234

which the energy required to increase the length of the domain wall (which separates the black bubble from its white surrounding) is offset by a gain in potential energy. However, we point out that these elongated states are observed only during the presence of the third domain and thus do not play a role in the part of the later trajectory that we analyze. The change of contrast of the tracked bubble (in particular compared to the stationary bubble) can have multiple reasons. Most notably, if the bubble shrinks in size below the spatial resolution, it appears less saturated in the image. That is, bubble breathing is a likely reason for the observed fluctuations of the colour saturation. Other possible reasons for the change of contrast include the motion of the bubble during the X-ray exposure and a small spatial variation of the position of the bubble during the 10^9 exposures corresponding to a given time delay. Hence, we cannot make fully conclusive claims on the origin of the contrast fluctuations. However, it should be emphasized, that while the existence of breathing is important for the behavior of the bubble, the strength of our analysis (and the reason we chose this theoretical approach) lies on the fact that we base our results on fitting the trajectory of the bubble. Therefore, our results remain robust.

Finally, we point out that the third domain does not retract to the notch at the edge of the disk before it disappears. Rather, the domain detaches from the edge and forms a third bubble in the bulk of the disk. In contrast to the other two bubbles, this bubble has a very short lifetime. The ability to annihilate shows that this bubble is not topologically protected. Thus, we conclude that this bubble has a Skyrmion number of $N = 0$ (the spin structure of an $N = 0$ bubble is depicted in the inset of Fig. 2a). It is remarkable that we were able to repeat such a creation and annihilation of an $N = 0$ bubble about 10^{10} times. This shows that we can control and investigate bubbles with different topology, which is not possible in materials with chiral Skyrmions (these are limited to $N = 1$ Skyrmions). Therefore, our experimental setup (including the material) is an ideal playground to study skyrmionic spin structures.

IV. TRAJECTORIES OF BUBBLES WITH VARIABLE $|N|$

Here we show that the dynamics of a Skyrmion, in particular its trajectory, is characteristic for its topology and its Skyrmion number N. We simulate the trajectories of bubbles with variable $|N|$, which allows us to identify the measured trajectory in the main paper with the simulated $|N| = 1$ bubble.

We have simulated the dynamic excitation and relaxation of $|N| = 0, 1, 2, 3, 4$ and 5 bubbles, using the parameters of Moutafis *et al.*[5] and the MICROMAGNUM simulation software.[10] Larger N Skyrmions (so called *hard bubbles*) are highly unlikely to be found in our material due to its small quality factor of $Q = 0.86(6)$.[13] Also, we start with energetically relaxed initial configurations, that is, we do not include any non-topological defects, such as non-winding vertical Bloch lines. While these defects can exist, they are very rare,[13] and are expected to annihilate during the first excitation.

The Skyrmion number N of the magnetisation configuration $\mathbf{m} = \mathbf{m}(x, y)$, where $\mathbf{m}$ is a unit vector along the local magnetisation, is calculated for all simulation steps by $N = (8\pi)^{-1} \int \mathrm{d}x\mathrm{d}y\, n$ with the topological density $n = \epsilon_{\mu\nu}(\partial_\mu \mathbf{m} \times \partial_\nu \mathbf{m}) \cdot \mathbf{m}$.[5,6] Note that the sign in this formula is not consistently defined in the literature, and that, for our definition and an axially symmetric structure with polarity p and winding number W, it can be simplified to $N = 1/2pW$.[5]

A spiralling trajectory, as observed in the measurements presented in the main paper, is only seen in the simulation of the $|N| = 1$ bubble. For all other topologies, the trajectories are more irregular: they cross themselves several times, and go through the potential minimum or spiral away from the equilibrium position in some instances. Therefore, we conclude that the observed trajectory in Fig. 2 of the main text corresponds to an $|N| = 1$ bubble.

We also note that, in contrast to the simulation in Fig. 2B, the measured trajectory in Fig. 3 of the main text is smooth and without spikes. This is due to the fact that, in the measurement, the higher frequency mode has a larger amplitude than the lower frequency mode at all times of the measured gyration. Due to the stronger damping of the higher frequency mode, the ratio of the amplitudes of the modes eventually reverses. The theoretical fit shows a transition to a hypocycloidal trajectory at $t = 16.2\,\mathrm{ns}$, accompanied by a change of the global sense of rotation from CW to CCW. The global amplitude at that stage is however expected to be smaller than 0.5 nm, which is below our spatial resolution and therefore cannot be observed experimentally.

DOI: 10.1038/NPHYS3234

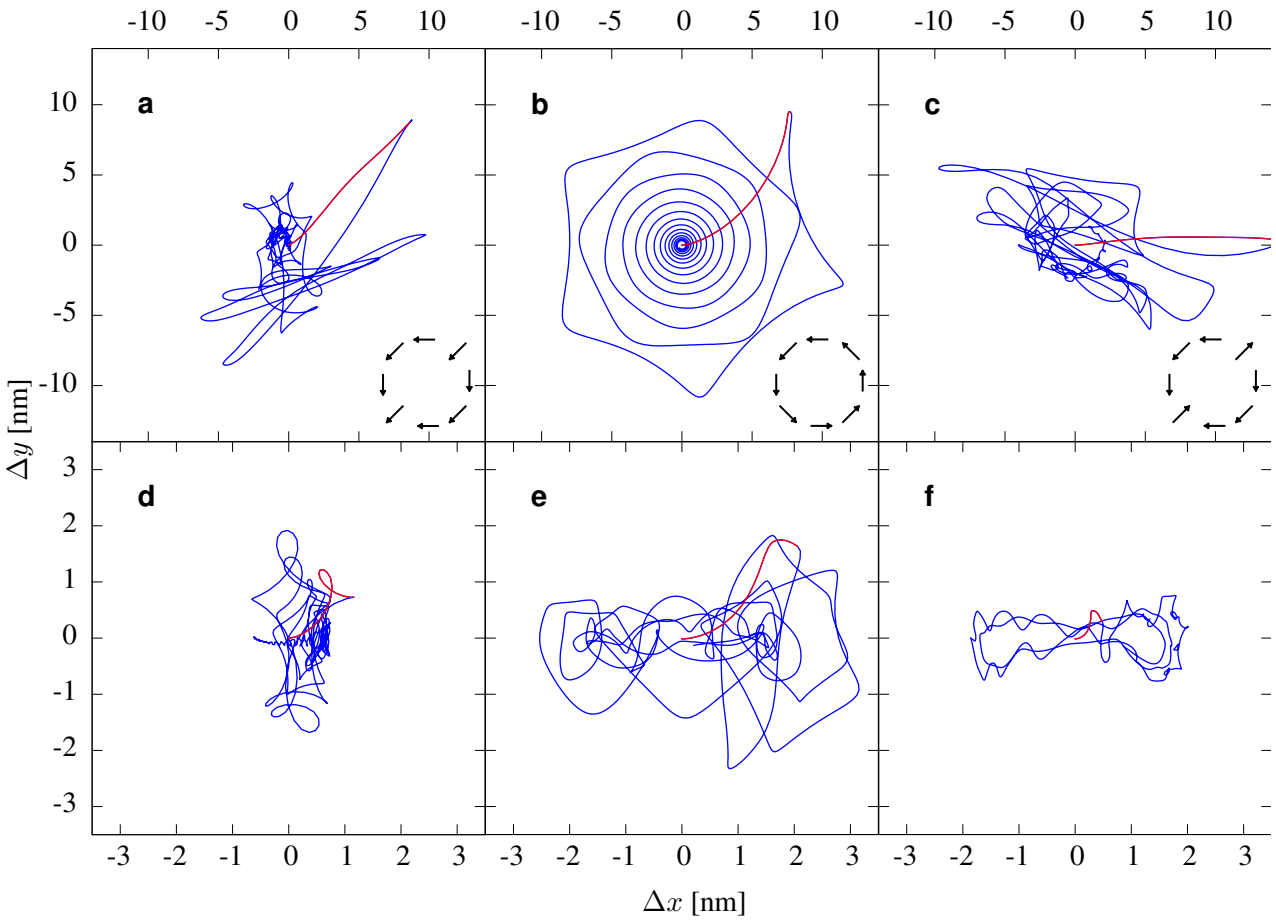

Figure 2 | Simulated trajectories of bubbles with variable Skyrmion numbers. Trajectories $(\Delta x, \Delta y)$ of the centre of magnetisation of the bubbles are shown for $|N| = 0$ in **a**, for $|N| = 1$ in **b**, for $|N| = 2$ in **c**, for $|N| = 3$ in **d**, for $|N| = 4$ in **e**, and for $|N| = 5$ in **f**,. The insets in **a–c** show configurations of the in-plane components of the spins of the bubble that correspond to the respective Skyrmion number. The simulations have been performed for negative N. For positive N, the trajectories are spatially inverted. Only the $|N| = 1$ bubble moves on a spiralling trajectory around the equilibrium position. The total simulation time is 15 ns. The excitation is applied for the first 0.2 ns, and the respective part of the trajectories is plotted with red lines.

V. SKYRMION GYRATION IN ANHARMONIC POTENTIALS AND UNDER THE APPLICATION OF EXTERNAL FIELDS

For our analysis of the observed Skyrmion gyration and, in particular, for determining the inertial mass, we use a parabolic approximation for the potential the Skyrmion moves in. To confirm the validity of our assumption and to check the general applicability of our results, we have simulated gyrating bubble Skyrmions in various kinds of realistic anharmonic potentials. These include: (i) gyrations in elliptically shaped elements of variable size simulating harmonic potentials with different potential stiffness along the x and y direction and (ii) gyrations in circularly shaped elements with periodic anisotropy modulations, simulating pinning with variable strength and lateral extent. Our simulations reveal that the impact of the anharmonic perturbations to the pinning potential on the inertial mass density are small and that the mass density can be reliably deduced using our model.

We furthermore simulated the gyration of bubble Skyrmions of variable size. We find that the mass density does not depend on the diameter of the Skyrmion, showing that the equation of motion is universal and remains unchanged when the Skyrmion moves through various geometries where confining potentials modify its equilibrium size.

A. Anisotropic harmonic potentials

To simulate anisotropic potentials, we utilize the fact that the bubble is repelled by the boundary of the magnetic element. We have simulated bubble gyrations in elliptical elements with variable semi axes s_x and s_y, following Suppl. IV and Ref. 5. In addition, we have applied magnetic bias fields in the perpendicular direction to modify the size of the bubble, similar to the real situation in the experiment. The maximum external field that we have applied is $4\,\mathrm{kA/m}$, which is slightly below the critical field at which the bubble collapses, so we probe the full parameter space.

As in the experiment, we determined the mass of the bubble by fitting its trajectory after the excitation is switched off (here for $t = 200\,\mathrm{ps}$) and thereby extracting the eigenfrequencies. The mass density is the mass divided by the domain wall area. As in the experiment, the domain wall is estimated by $2t_{\mathrm{Film}}\sqrt{\pi A}$, where t_{Film} it the film thickness and A is the surface area of the bubble. The resulting mass densities (normalized to

DOI: 10.1038/NPHYS3234

H [kA/m]	s_x [nm]	s_y [nm]	$\rho_m/\rho_{m,0}$
0	80	80	1.00
0	100	80	0.98
0	100	100	1.01
40	80	80	0.97
40	100	80	1.00
40	100	100	0.99

Table I | Mass densities ρ_m of bubbles in elliptical potentials. The mass density is listed as a function of external bias field H and elliptical semi axes s_x and s_y of the confining element. The mass density is normalized to the mass density of a bubble in a circular disk of $80\,\mathrm{nm}$ radius without applied field (first line).

the mass of case 1, the unperturbed bubble in a circular disk) can be found in table I. The data reveals that the mass density of the bubble neither depends on the size of the bubble nor on the anisotropy of a harmonic confining potential.

B. Anharmonic potentials – the impact of pinning

In section III, we have argued that there is substantial pinning present in our magnetic element. In fact, we utilize the pinning (and not the boundary of the element) to confine the motion of the bubble and study its relaxation on a gyrotropic trajectory. In our analysis, we have assumed the pinning potential to be parabolic. The excellent agreement of the data with this model is a strong indicator for the validity of this assumption. However, the real potential will have some anharmonic component, and it is *a priori* unclear how large the error for the determined mass is that is caused by such anharmonic perturbations.

To mimic pinning-like fluctuations of the potential, we have simulated gyrating bubbles in many magnetic elements with a variety of spatially dependent perpendicular anisotropy distributions

$$K = K_0 + \Delta K \cos(2\pi x/\lambda)\cos(2\pi y/\lambda), \tag{2}$$

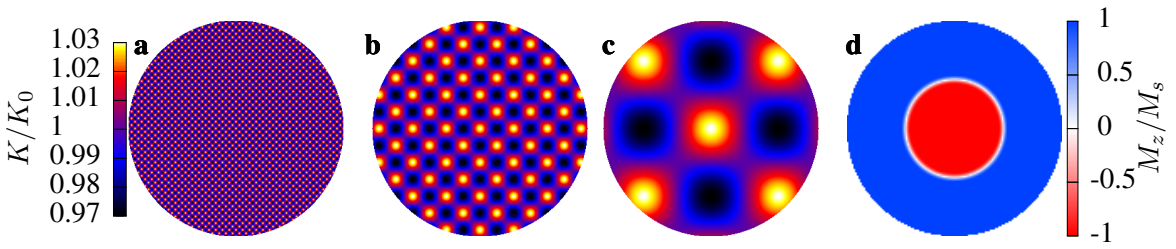

Figure 3 | Initial configurations for the simulations. a-c, Periodic modulations of the perpendicular anisotropy, mimicking pinning on all relevant length scales (examples show configurations for $\lambda = 5\,\mathrm{nm}$ in **a**, for $\lambda = 25\,\mathrm{nm}$ in **a**, and for $\lambda = 100\,\mathrm{nm}$ in **c**). **d**, Initial magnetic configuration in the disk. All simulations are started with a bubble of $36\,\mathrm{nm}$ radius centered in the disk of $80\,\mathrm{nm}$ radius

where K_0 is the anisotropy constant of the homogeneous material, ΔK is the strength and λ is the wavelength of the modulation. Simulations were performed for values of $\Delta K/K$ between $3\,\%$ and $10\,\%$ and periodicities λ between $5\,\mathrm{nm}$ and $100\,\mathrm{nm}$, which is in line with possible structural variations causing such anisotropy modulation (such as given by grain size, surface roughness, lithography patterning precision, disk diameter, etc.).[11] With a bubble radius of $36\,\mathrm{nm}$ and a maximum excursion of $10\,\mathrm{nm}$, the chosen values for λ cover all important length scales, and a anisotropy variation of $\pm 10\,\%$ is more than we would expect in our low pinning material.[12] Examples of the anisotropy modulations are depicted in Fig. 3, where the colour encodes the anisotropy strength.

In Fig. 4, we plot the mass density (normalized to the mass of the unperturbed bubble) as a function of the modulation strength and modulation wavelength. As in the experiment, we use the two frequency harmonic model to fit the simulated trajectories, as shown in Fig. 5. As in the experiment we use the extracted frequencies to obtain the mass density for different pinning (the combinations of pinning strength and lengthscale for which we extracted this information are shown in Fig. 4). We do not consider data where only one mode is present (quantitatively, if the other mode has an initial amplitude of smaller than $1\,\mathrm{nm}$), because both modes are required to determine the mass and two modes are present in the experiment.

The main observation that can be obtained from Fig. 4 is that the impact of the exact pinning details (strength and periodicity of the anharmonic potential) on the mass density is very small. We thus conclude that our analysis of realistic deviations of the pinning potential from the harmonic approximation shows that

DOI: 10.1038/NPHYS3234

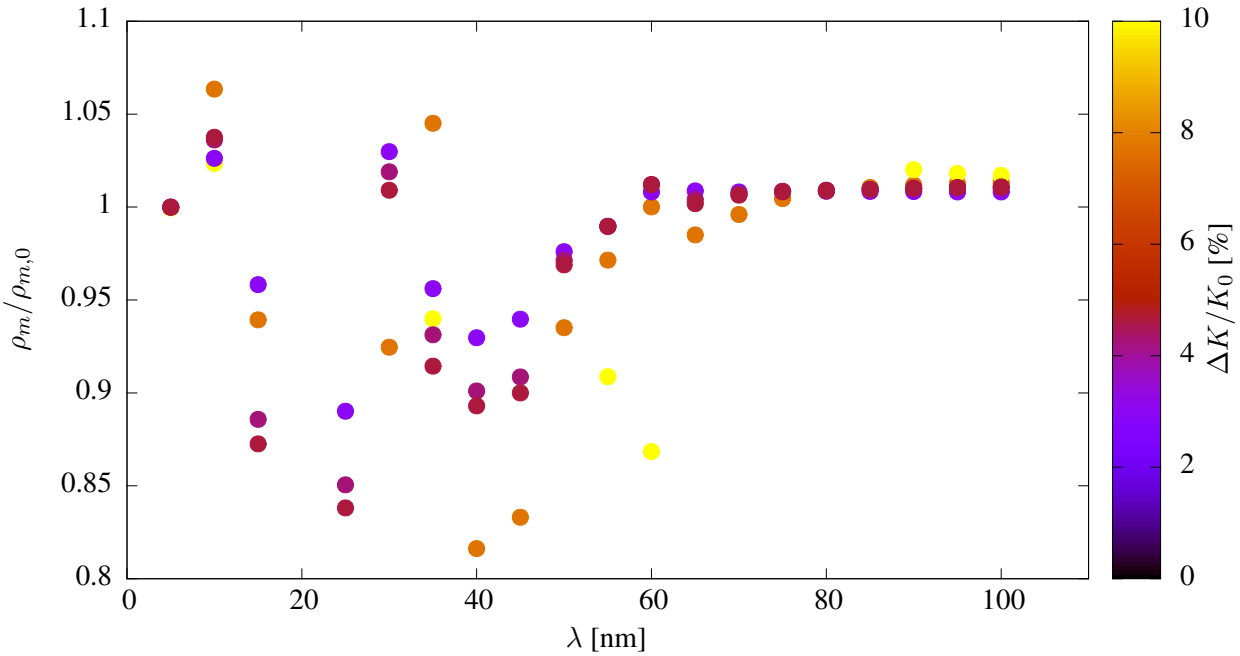

Figure 4 | Bubble mass density as a function of pinning length scale and strength. The graph shows the mass density of the bubble ρ_m determined using the method presented in the main article as a function of pinning modulation periodicity λ and pinning strength ΔK. Mass and pinning strength are normalized to the unperturbed mass $\rho_{m,0}$ and the average perpendicular anisotropy constant K_0, respectively.

the lower limit for the mass density derived from the experimental data is reliable. Our method to determine the mass is thus robust against pinning details and does not rely on the harmonicity of the potential. Therefore, the lower limit for the mass density is a universal constant of our particular material; it neither depends on pinning, nor on the shape of the magnetic element, nor on any other perturbations of the local potential.

C. Skyrmion motion under the application of external fields

In the main paper we claim that the large mass of the Skyrmion originates in the storage of energy through a variation of the Skyrmion's size. Naturally, this leads to the question how the mass depends on the size of the Skyrmion. To answer this question, we have performed simulations of gyrating bubbles in a static external magnetic field that alters the equilibrium diameter of the bubble. Essentially, we find that the mass density

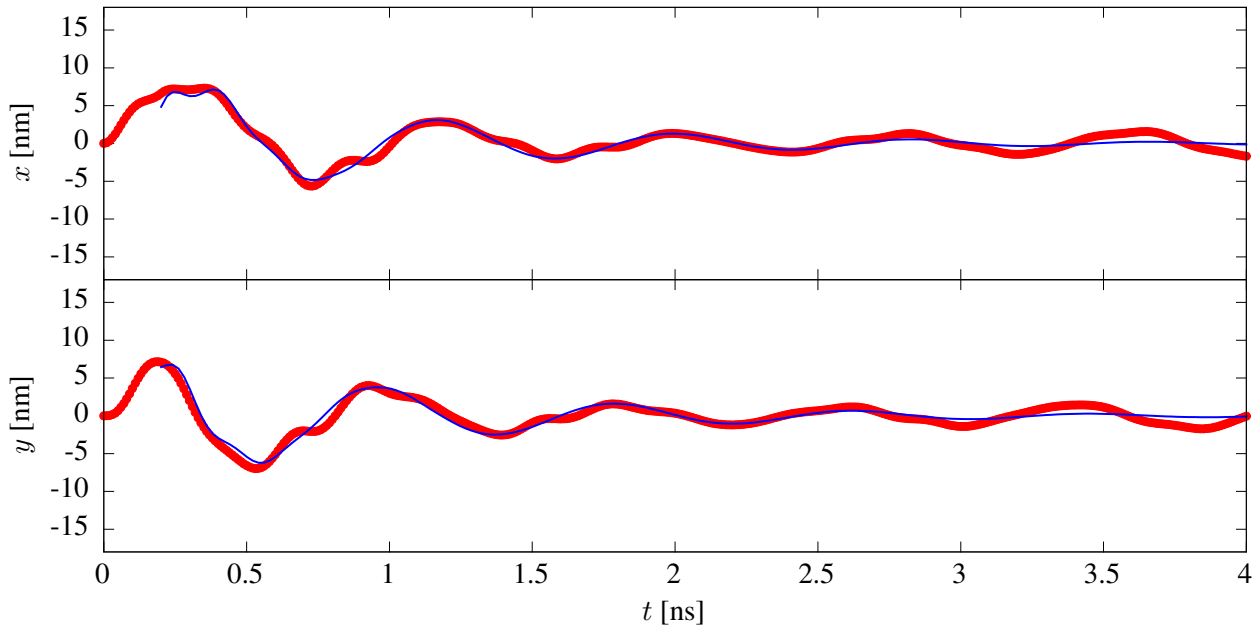

Figure 5 | Bubble trajectories that show good agreement with the theoretical model. The graph shows the trajectory for $\Delta K/K = 10\,\%$ and $\lambda = 60\,\mathrm{nm}$. The trajectory shows clear deviations from a pure sine wave, i.e., both eigenmodes are present with a considerable amplitude. The theoretical model is able to describe the data well.

is independent of the actual size of the bubble, see Fig. 6. The variation of the mass density with the bubble radius is smaller than 3 % within the whole stability range of the bubble. That means that the equation of motion does not change when a Skyrmion moves in various geometries, where confining potentials can alter the size of the Skyrmion, i.e., the equation of motion is universal.

DOI: 10.1038/NPHYS3234

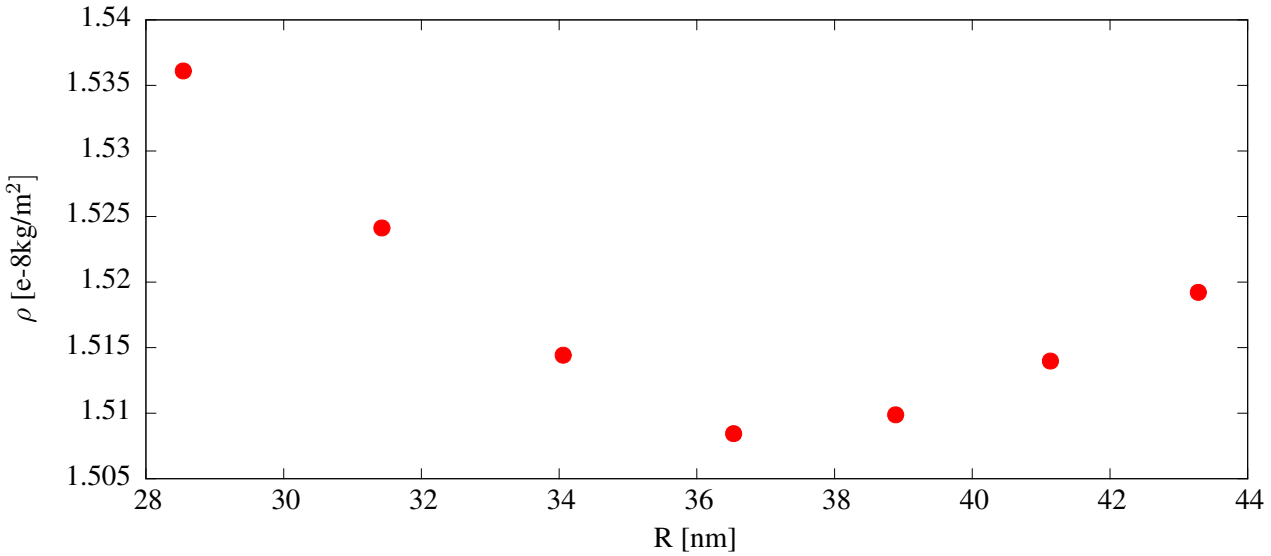

Figure 6 | Evolution of the inertial mass density of a bubble Skyrmion as a function of its radius. The mass density was derived from the frequencies of a simulated gyrotropic motion. The radius of the bubble at rest R was varied using a global static out-of-plane bias magnetic field. Smaller or larger radii are unstable with the used simulation parameters and geometry.

VI. DETERMINATION OF THE DÖRING MASS DENSITY

The Döring mass is so far the only known source of inertia in magnetism. This concept is based purely on local magnetostatic energies. Here we calculate the magnitude of the Döring mass for our material and show that non-local contributions have to be considered for explaining the inertia of skyrmionic spin structures, as these non-local terms dominate the effective mass measured here.

The Döring mass density m_D of a straight Bloch domain wall is calculated via $m_D = M_s^2(1+\alpha^2)/(K_\perp \gamma^2 \Delta_0)$.[13] Here, α is the viscous (Gilbert) damping, $\Delta_0 = \sqrt{A/K_{u,\mathrm{eff}}}$ is the domain wall width parameter of a Bloch wall with exchange stiffness A and effective out-of-plane anisotropy constant $K_{u,\mathrm{eff}}$, and $K_\perp$ is the transverse anisotropy constant associated with a small tilt of the in-plane angle ψ of the spins from the energetically favourable $\psi = 0$ Bloch wall towards the unfavourable $\psi = \pi/2$ Néel wall. This anisotropy $K_\perp$ is often approximated by $K_\perp = \mu_0 M_s^2/2$,[13] which is, however, only valid for a single domain wall in an infinite, uniform, and magnetically homogeneous sample. For our multilayer stacks of finite thickness, we obtain $K_\perp$

from numerically solving its stray field integral, only assuming a Bloch wall of the same width Δ_0 in each layer. For our specific multilayer stack, we find $K_\perp = 0.07(2)\mu_0 M_s^2$, which is comparable to the effective out-of-plane anisotropy $K_{u,\mathrm{eff}} = 0.09(1)\mu_0 M_s^2$. The in-plane tilt of the spins in the top- and bottommost layers leads only to minor corrections to this result (increase of the mass density by less than 20 % if 10 of the 30 layers are fully in-plane magnetised).

Superconducting quantum interference device (SQUID) measurements of our material yield a saturation magnetisation of $M_s = 1.19(3) \times 10^6\,\mathrm{A/m}$. The Bloch domain wall width parameter Δ_0 is determined by the comparing small angle X-ray scattering (SAXS) Bragg peaks of a stripe domain continuous film of our magnetic multilayer with the scattering from a simulated domain profile. We find $\Delta_0 = 11(2)\,\mathrm{nm}$. For the damping we assume a conservative (i.e., large) estimate of $\alpha = 0.2$, based on previous studies on similar Co/Pt multilayers.[15] With all these parameters, we arrive at a Döring mass density of $m_D = 3.5(8) \times 10^{-8}\,\mathrm{kg/m^2}$, which is (within the error bars) a factor five smaller than the mass density of the bubble. A similar difference in mass density between theoretical calculations and numerical simulations has been reported before,[6] but the discrepancy could not be explained. What we demonstrate here is that the larger mass originates from a non-local contribution to inertia that arises from the Skyrmion topology.

VII. SKYRMION IN A WIRE

In the following section, we discuss the application of our Skyrmion particle model for the case of a wire geometry model, which has recently been proposed as a memory device,[16] in particular after the nucleation and annihilation of Skyrmions became under control.[17–19] In particular, we show the impact of the mass term on this kind of dynamics.

We assume a magnetic wire in x direction with a confining parabolic potential in y direction (with stiffness K). A driving force $F(t)$ acts on the x position of the Skyrmion. The Skyrmion motion, according to Eq. (1), is then given by

$$M\ddot{x} - G\dot{y} + D\dot{x} = F(t) \tag{3}$$

$$M\ddot{y} + G\dot{x} + D\dot{y} + Ky = 0, \tag{4}$$

where the parameters $M, G,$ and D are the Skyrmion mass, the z component of the gyrovector, and

DOI: 10.1038/NPHYS3234

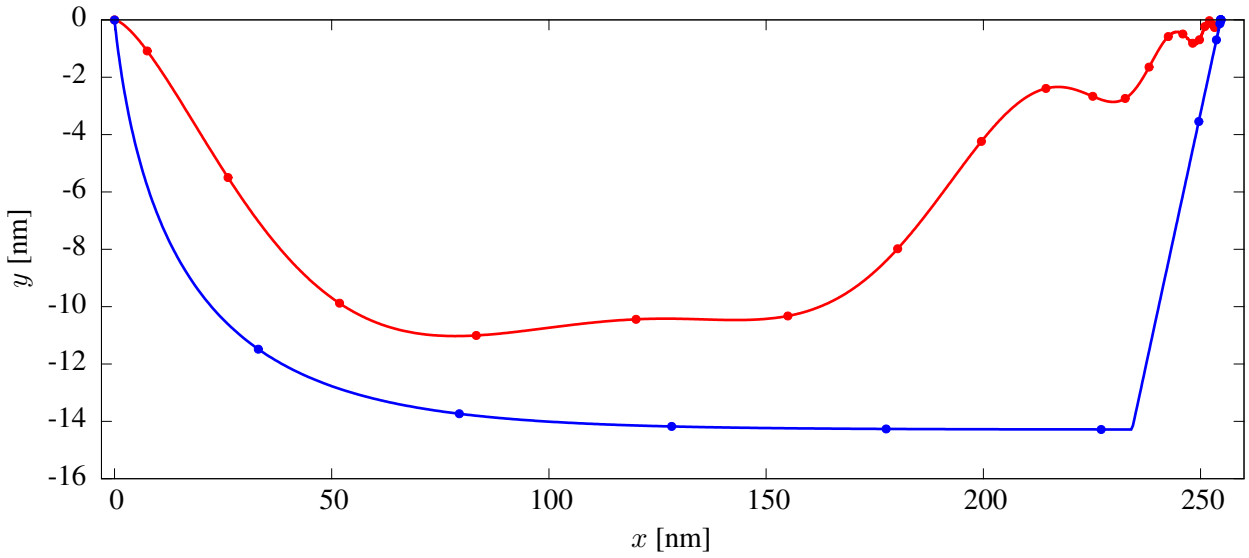

Figure 7 | Simulated mass-dependent trajectories of Skyrmions in a wire. The graph shows the trajectories of two Skyrmions, one massive (red line) and one massless (blue line). Both Skyrmions start at $(0, 0)$ and propagate to the right (positive x). Points along the lines indicate the position in time steps of $1\,\mathrm{ns}$. Both Skyrmions travel the same distance, but the massless one propagates significantly further perpendicular to the wire axis.

the damping, respectively. We choose, consistent with our experimental data, $M = 2 \times 10^{-21}\,\mathrm{kg}, G = 10^{-12}\,\mathrm{kg/s}, D = 7 \times 10^{-13}\,\mathrm{kg/s}$, and $K = 3.5 \times 10^{-3}\,\mathrm{N/m}$ (M and D are estimates from the lower limits determined in the experiments). We move the Skyrmion, initially at rest, with a $t_p = 5\,\mathrm{ns}$ long and $F = 3.5 \times 10^{-11}\,\mathrm{N}$ strong single rectangular-shaped driving force pulse (where the strength is estimated to yield a maximum velocity $v_{x,\mathrm{max}} = F/D$ of $50\,\mathrm{m/s}$). We plot the trajectory of this Skyrmion in Fig. 7, alongside with that of a massless Skyrmion under the same conditions.

We observe, in agreement with micromagnetic simulations,[17] that the Skyrmion is deflected perpendicular to the wire axis (y direction). This is the effect of the gyrocoupling vector. The Skyrmion exponentially approaches its equilibrium y position with a characteristic time constant τ_y. A massive Skyrmion shows additionally small oscillations on this way, which we do not discuss in detail as it is not relevant for the displacement that we are interested in. After approaching equilibrium, the Skyrmion moves with a constant velocity in x direction, until the driving force is switched off. Directly afterwards, the velocity in x is ex-

ponentially damped off, and in y direction the Skyrmion returns to $y = 0$ with an exponential function, see Fig. 8.

We find, by analyzing trajectories for a large set of variable parameters M, G, D, K, F, and t_p, that there is one single time constant for the motion in y direction, τ_y, and one for the motion in x direction, τ_x. We furthermore find that the numerical solutions can be well approximated by

$$\tau_x = \frac{M}{D} + \frac{G^2}{KD} \tag{5}$$

$$\tau_y = \frac{M}{D} + \frac{G^2}{KD} + \frac{D}{K} + f(M, D, G, K) \tag{6}$$

$$x(t) = \begin{cases} \frac{F}{D}t - \frac{F}{D}\tau_x \left(1 - \exp\left(-t/\tau_x\right)\right) & t <= t_p \\ x(t_p) + \frac{F}{D}\tau_x \left(1 - \exp\left(-t_p/\tau_x\right)\right)\left(1 - \exp\left(-(t - t_p)/\tau_x\right)\right) & t > t_p \end{cases} \tag{7}$$

$$y(t) \approx \begin{cases} -\frac{GF}{KD}\left(1 - \exp\left(-t/\tau_y\right)\right) & t <= t_p \\ y(t_p)\exp\left(-(t - t_p)/\tau_y\right) & t > t_p \end{cases} \tag{8}$$

where the function $f(M, D, G, K)$ is zero for $M = 0$ and small compared to the other contributions to τ_y elsewhere. The $\approx$ sign means that we neglect the small oscillations in y. From these analytical trajectories we can read the scaling for the propagation length x_{max} of the Skyrmion and for its maximum displacement y_{max} perpendicular to the wire:

$$x_{\text{max}} = \frac{F}{D}t_p \tag{9}$$

$$y_{\text{max}} = -\frac{GF}{KD}\left(1 - \exp\left(-t_p/\tau_y\right)\right). \tag{10}$$

The displacement perpendicular to the wire becomes problematic as soon as the Skyrmion approaches the edge of the wire and thus risks being expelled. In an application, one therefore has to define a critical displacement y_{crit} that must not be exceeded in order to guarantee that no Skyrmion is lost. If $y_{\text{crit}} < y_{\text{max}}$, i.e., for short and strong driving forces, we can use Eq. (10) to derive the maximum pulse length $t_{p,\text{max}}$ that is still in agreement with the constraint on y_{max}, as illustrated in Fig. 8. From $t_{p,\text{max}}$ we directly obtain the associated

DOI: 10.1038/NPHYS3234

Skyrmion propagation $x_{\max}$:

$$t_{p,\max} = \tau_y \ln\left(\frac{1}{1-\left|y_{\text{crit}}\frac{KD}{GF}\right|}\right) \tag{11}$$

$$x_{\max} = \tau_y \frac{F}{D} \ln\left(\frac{1}{1-\left|y_{\text{crit}}\frac{KD}{GF}\right|}\right). \tag{12}$$

Under the given constraint of a maximum tolerable transversal displacement, the longitudinal propagation of a Skyrmion scales linearly with the time constant τ_y. For the Skyrmion investigated in the main paper, $G^2/K = 2.9 \times 10^{-22}\,\text{kg}$ and thus the large mass term found by us dominates both time constants according to $\tau_x \approx \tau_y \approx \tau := M/D$, and thus $x_{\max} \propto M$. That is, the mass of a Skyrmion leads to a centrifugal force that is important to avoid the Skyrmions from being expelled when moved with short and strong excitations along a wire. With the correct quasi-particle model for magnetic Skyrmions provided here, it is now possible to obtain analytical expressions for the motion of Skyrmions. Such direct and accurate understanding of the effect of all parameters is key to determine which parameters should be tuned in order to produce a device with a certain behaviour.

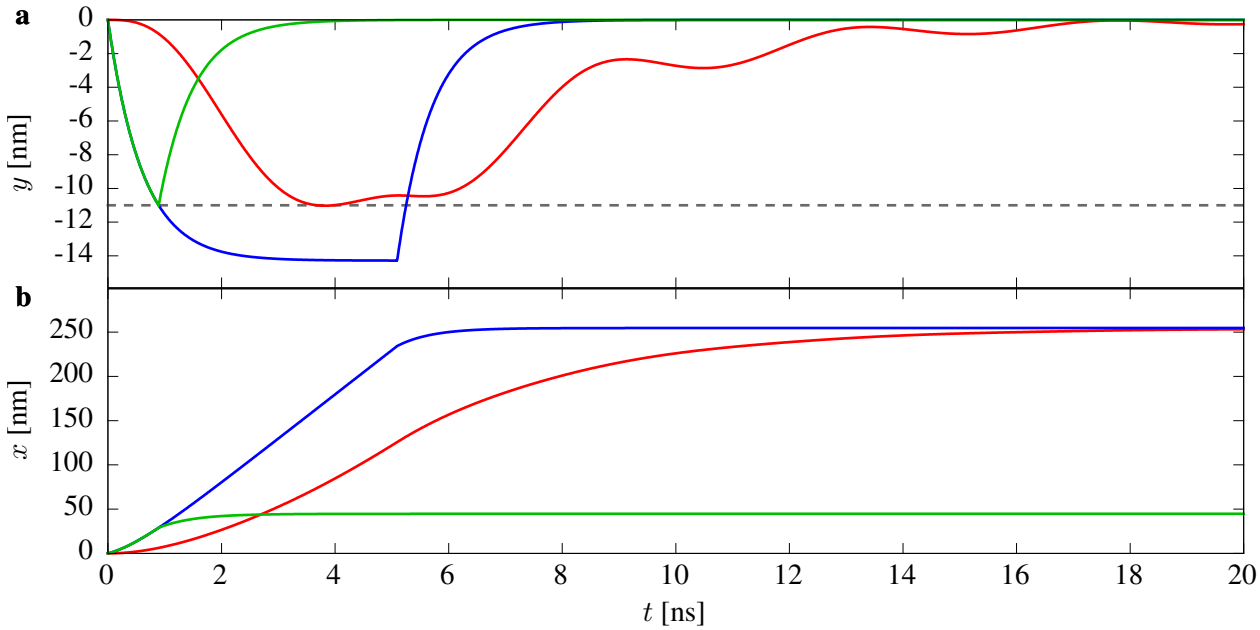

Figure 8 | Simulated trajectories of Skyrmions in a wire with critical transverse displacement. a, Transverse displacement $y(t)$ and **b**, longitudinal propagation $x(t)$. The critical transverse displacement y_{crit} is sketched with the grey dashed line in (**a**). The red line depicts the trajectory of a massive Skyrmion that is displaced by a $t_p = 5\,\text{ns}$ long and $F = 3.5 \times 10^{-11}\,\text{N}$ strong pulse. The maximum transverse displacement is below the threshold. The blue line shows the trajectory of a massless Skyrmion, moved by the same pulse. Now, the Skyrmion moves significantly over the threshold. To ensure that the Skyrmion is not expelled from the wire, the pulse must be shorter (or weaker). The green line plots the trajectory of a massless Skyrmion, excited with a $t_p = 0.9\,\text{ns}$ long pulse. Now, the Skyrmion remains within the transverse tolerances. The propagation along the longitudinal direction, however, is much shorter for the massless Skyrmion than for the massive one, if both obey the restriction in y. The same holds if one reduces the pulse strength instead of the pulse length.

VIII. EXPERIMENTAL METHODS

The sample was prepared as described in Refs. 12 and 14. The sample consists of a 350 nm thick silicon nitride membrane of approximately $3\,\mu\text{m} \times 4\,\mu\text{m}$ lateral dimensions. The back side of this membrane is covered with a $[\text{Cr}(5)/\text{Au}(55)]_{20}$ (thickness in nm) multilayer to block the incident X-rays (X-ray transmission

DOI: 10.1038/NPHYS3234

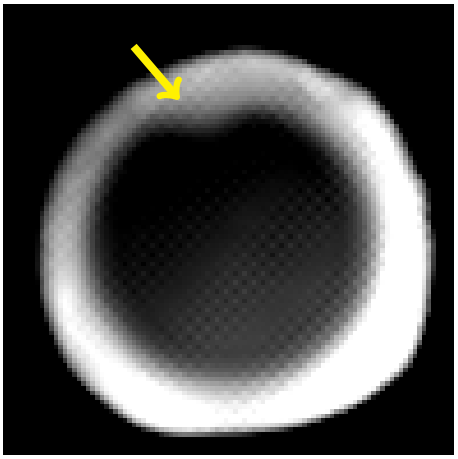

Figure 9 | Sample topography as visible by the imaging X-rays. White indicates high X-ray transmittance, black indicates high absorption. The object hole appears as a bright white circle. Within the object hole the magnetic disk is found (dark gray). The disk is a circle with a small notch at the top, as indicated by the yellow arrow.

at the used photon energy of 778 eV is less than 10^{-7}). Three holes are etched in this layer down to the silicon nitride membrane, comprising the object hole (800 nm wide) and two reference holes (50 nm diameter), approximately 2 µm to 3 µm away from the object hole.

On the front side of the membrane, several features are prepared, aligned with respect to the object and reference holes. Directly behind the object hole, a magnetic disk with 550 nm diameter with a small notch at the top is positioned, see Fig. 9. The magnetic material is a Pt(2)/$[Co_{68}B_{32}(0.4)/Pt(0.7)]_{30}$/Pt(1.3) (thickness in nm) multilayer, which has been shown to be particularly suitable for pump-probe dynamic imaging of intrinsically out-of-plane magnetised structures.[12]

Next, a Au nanowire with a 300 nm×300 nm square cross section is laid around the disk for magnetic excitation. The cross section of this wire is chosen to achieve a 50 Ω impedance, ensuring optimal transmission of high frequency current pulses. The Au nanowire is shaped to a microcoil of 760 nm inner diameter, i.e., as tight as possible to the magnetic disk to generate a maximum magnetic field with a given current through the coil. A current flowing through this microcoil generates a magnetic field at the position of the disk that is reasonably uniform. The direction of the generated magnetic field is almost purely out-of-plane (z-direction).

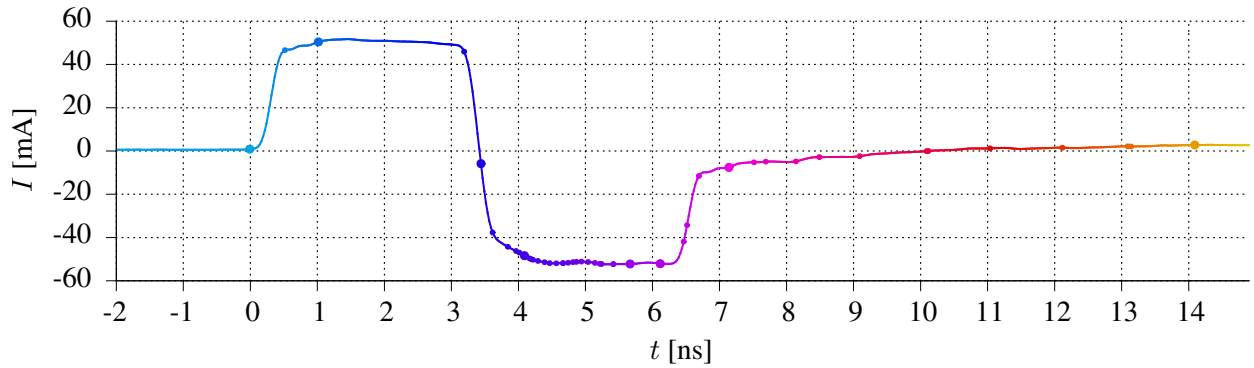

Figure 10 | Current pulse sent through the microcoil to excite the bubble dynamics. A positive current generates a field that is favoring the magnetisation orientation inside the bubbles (black), whereas a negative current generates a magnetic field that favors the white area surrounding the bubbles. Each coloured point represents an acquired image and larger dots represent the images shown in Fig. 2c of the main paper.

The perpendicular anisotropy of the sample is not perfectly homogeneous. The anisotropy variation leads to a modulation of the energy landscape for the presence of domain walls. That is, the energy of domain walls is lower in some regions of the sample than in others. Hence, bubble domains are more likely to form in these regions of lowest domain wall energy. We have utilized this effect to create a state with two bubbles at deterministic rest positions by increasing the static external field slowly until all domains at positions of higher energy have disappeared. The resulting field was −120 mT. At higher fields, all domains eventually disappear and the sample attains to the uniform ferromagnetic state. At lower fields, more bubble domains appear and elongate to stripe domains.

During the experiment, we injected bipolar current pulses with a current of ±52 mA through the microcoil. The pulse shape is plotted enlarged in Fig. 10 and numerical data is provided in Table II. At maximum current, this pulse creates a field at the position of the tracked bubble of $B_z = \pm 35\,\mathrm{mT}$ in the out-of-plane direction, with a small in-plane component of $B_x = -1.5\,\mathrm{mT}$ and $B_y = 6.5\,\mathrm{mT}$. The residual field gradient was $\partial_x B_z = 8.7\,\mu\mathrm{T/nm}$ and $\partial_y B_z = -45\,\mu\mathrm{T/nm}$, pushing the bubble towards the centre of the disk.

Images of the induced bubble motion were recorded using time-resolved X-ray holography. Magnetic images were obtained by illuminating the sample with circularly polarized X-rays at an energy tuned to the Co L_3 resonance (778 eV photon energy). At this energy, right-circularly polarized photons (positive helicity)

DOI: 10.1038/NPHYS3234

t [ns]	x [nm]	y [nm]	t [ns]	x [nm]	y [nm]	t [ns]	x [nm]	y [nm]
−14.41(5)	−1(2)	−2(2)	4.46(5)	−23(2)	−9(2)	6.46(5)	15(2)	−1(1)
0.00(5)	**−3(1)**	**0(1)**	4.56(5)	−19(1)	−9(1)	6.52(5)	16(3)	−1(6)
0.51(5)	0(2)	−8(1)	4.66(5)	−17(1)	−2(9)	6.68(5)	22(2)	−4(2)
1.02(5)	**−22(2)**	**−21(3)**	4.67(5)	−15(3)	−6(2)	7.15(5)	10(1)	−12(2)
3.20(5)	−33(1)	−42(3)	4.75(5)	−15(3)	−7(3)	**7.15(5)**	**14(1)**	**−12(2)**
3.43(5)	−33(3)	−43(2)	4.81(5)	−19(2)	−11(1)	7.51(5)	8(2)	−12(2)
3.44(5)	**−34(2)**	**−40(3)**	4.86(5)	−16(2)	−9(3)	7.69(5)	2(2)	−8(3)
3.63(5)	−30(2)	−36(2)	4.93(5)	−11(3)	−1(5)	8.14(5)	−1(2)	−6(2)
3.84(5)	−21(1)	−27(3)	5.04(5)	−11(2)	−3(2)	8.48(5)	−2(2)	−7(1)
3.96(5)	−30(1)	−21(2)	5.14(5)	−13(2)	5(4)	9.10(5)	−4(2)	−3(2)
4.01(5)	**−25(1)**	**−20(1)**	5.23(5)	−11(3)	3(2)	10.10(5)	−4(2)	−1(1)
4.10(5)	−25(2)	−16(2)	5.24(5)	−8(2)	3(2)	11.05(5)	−1(2)	−2(2)
4.17(5)	−25(2)	−16(3)	5.43(5)	−6(3)	9(4)	12.12(5)	−2(1)	−5(2)
4.19(5)	−23(2)	−16(2)	5.43(5)	−3(2)	4(2)	13.10(5)	1(4)	3(5)
4.22(5)	−22(1)	−15(1)	**5.67(5)**	**0(5)**	**7(2)**	13.14(20)	7(2)	−1(2)
4.29(5)	−18(1)	−9(2)	**6.13(5)**	**15(2)**	**5(3)**	**14.10(5)**	**3(1)**	**−2(2)**
4.38(5)	−21(2)	−9(1)	6.14(5)	17(2)	8(8)			

Table II | Numerical values of the trajectory of the bubble, including estimated errors (standard deviation). The data points corresponding to the images shown in Fig. 2c of the main paper are printed bold.

are absorbed more (less) if the magnetisation of the sample is parallel (anti-parallel) to the photon propagation direction. The reverse is true for left-circularly polarized photons (negative helicity). This effect is called X-ray magnetic circular dichroism. Hence, if we record a transmission image of the sample at this energy with right and with left circular polarisation and subtract the images, we obtain an image with purely magnetic information, where regions of positive net transmission (white) indicate that the magnetisation is pointing

anti-parallel to the propagation direction of the incident beam, whereas regions of negative net transmission (black) indicate that the magnetisation is pointing in the opposite direction. This is how the magnetic images shown are to be interpreted.

To obtain such a transmission image, we use X-ray holography, i.e., we record the far field scattering pattern of the transmitted photons. This far field scattering pattern is related to the sample transmission function through a Fourier transform. This Fourier space information is complex-valued, while the detector can only record the amplitude. To measure the phase information, which is vital for a successful reconstruction of the original transmission function, the two small reference holes serve as point-like sources for reference beams. The interference of these reference beams with the primary beam from the magnetic sample shifts the phase information to a detectable amplitude modulation. The reconstruction of such a hologram is then obtained via a single inverse Fourier transform.[20]

Time-resolved imaging was achieved by using short (50 ps long) bunches of X-rays with a precisely defined repetition rate. We used the exact same repetition frequency for the injected current pulses, such that the X-rays arrived always at precise time delay with respect to the start of the current pulse. To obtain an image with good contrast, we had to integrate over approximately 10^9 X-ray pulses.

The images of the movie were recorded one-by-one. That is, after completing the recording of an image corresponding to time delay t_1, we changed the arrival time of the current pulse to record another image corresponding to a time delay t_2. The series $\{t_1, t_2, t_3, ..., t_n\}$ was chosen non-chronologically (e.g., $t_3 < t_1 < t_2$) to ensure that the changes between succeeding frames in the time-sorted movie are truly dynamical.

One major advantage of X-ray holography is that the imaging is inherently insensitive to drift: because the reconstruction of the real space information involves a Fourier transform of the recorded data, a drift of the sample with respect to the detector translates to a pure phase shift in the reconstruction. That is, a drifting or vibrating sample reduces the overall contrast (because the final image is an average of many images that are slightly phase-shifted with respect to one another), but the location of the reconstructed information does not change.

DOI: 10.1038/NPHYS3234

IX. DATA ANALYSIS

We have used the absence of drift to track the motion of the bubble with extremely high accuracy. The bubble is defined as a region of connected pixels with common below-average intensity (i.e., pixels which appear black in the image). The centre of the bubble is obtained by calculating the first statistical moment (centre of "mass") of all pixels of the bubble. This statistical method determines the centre with much higher accuracy than the actual spatial resolution (which is about 40 nm for the reconstruction of the smaller reference hole in our case[14]). The tracking precision is set by a statistical average and limited only by the noise level. Since noise in X-ray holographic reconstructions has generally a long periodicity, the noise variation across the bubble is small. We estimate the precision (i) by evaluating the reconstructions from both references independently and assuming that the difference corresponds to one standard deviation, and (ii) by adding a conservative estimate of the average spread of the data of 1.4 nm (which was derived by assuming a linear trajectory in the time interval $t \in [3.44\,\mathrm{ns}, 5.67\,\mathrm{ns}]$ and by calculating the standard deviation of the data from a linear fit). This results in an average spatial accuracy of 2.3 nm for the determination of the centre of the bubble.

The bubble trajectory is described by Eq. (1) of the main article. The solution of this equation of motion is a coherent superposition of two damped oscillations (with eigenfrequencies $\omega_{1,2}$, damping time constants $\tau_{1,2}$, and complex amplitudes $A_{1,2}$) around an equilibrium position r_0:

$$r(t) = A_1 \exp(i\omega_1 t - t/\tau_1) + A_2 \exp(i\omega_2 t - t/\tau_2) + r_0(t), \tag{13}$$

Here, the vector $\mathbf{R} = (X, Y)$ is conveniently parametrised by the complex number $r = X + iY$. The equilibrium position r_0 is time-dependent due to an effective dynamical magnetic field gradient during the pulse. The two amplitudes of the gyrotropic modes are defined by the initial position and velocity. All parameters of Eq. (13) are determined from a fit to the experimental data, which is visualised by a coloured, solid line in Fig. 3 of the main article.

In the fit, data points with $t < 6\,\mathrm{ns}$ are weighted by half to compensate for the fact that there are significantly more data points in that region than at larger time delays. We include only data from the gyrotropic part of the trajectory (data points with $t > 4.5\,\mathrm{ns}$). As outlined in the Supplemental Material of Ref. 6, the ratio of the damping strengths equals the ratio of the respective frequencies, that is, $\tau_2 = \tau_1\omega_1/\omega_2$. The

equilibrium position r_0 is shifted by a field gradient. The applied field pulse, of which only the negative part coincides with the fit interval, has a weak gradient, and more significantly, the negative B_z during the pulse causes a modification of the sample magnetisation, in particular a shrinking of the second bubble. The modification of the stray field due to this shrinking leads to an effective field gradient of known direction $\partial_x B_z^{(b)}/\partial_y B_z^{(b)} = -1.5, \partial_x B_z^{(b)} > 0$, as determined from the observed positions of the two bubbles, but unknown strength. For simplicity, we assume instantaneous modification of the second bubble by the field pulse, and we approximate the pulse by a step function with a step at $t_1 = 6.45\,\mathrm{ns}$, which equals the time where the real pulse decays to half its maximum value after being switched off. We therefore have two distinct constant values $r_1 := r_0(t < t_1)$ and $r_2 := r_0(t \geq t_1)$, the latter corresponding to the static equilibrium position, which is determined from the average of all positions after $t > 9.5\,\mathrm{ns}$. The value for r_1 is obtained from a fit to the data, and we constrain the parameters A_1 and A_2 for the two fit regions $t < t_1$ and $t \geq t_1$ to ensure the continuity of the total function in its value and its first derivative. We obtain the best fit with $\omega_1 = 1.00(13)\,\mathrm{GHz}$, $\tau_1 = 3.2(6)\,\mathrm{ns}$, $\omega_2 = -1.35(16)\,\mathrm{GHz}$, $\tau_2 = 2.3(6)\,\mathrm{ns}$, and $r_1 = x_1 + iy_1$ with $x_1 = 5.1(8)\,\mathrm{nm}$ and $y_1 = -10.2(15)\,\mathrm{nm}$.

The determined frequencies can be used to calculate the mass M of the bubble and the potential stiffness K. Specifically, the equation of motion of the bubble (Eq. (1) of the main paper) can be written in scalar complex coordinates r as

$$-M\ddot{r} + (D + iG)\,\dot{r} - Kr = 0. \tag{14}$$

This is the equation of a damped harmonic oscillator, with the well-known solution

$$r(t) = A\exp(i\bar{\omega}_1 t) + B\exp(i\bar{\omega}_2 t) \tag{15}$$

with

$$\bar{\omega}_{1,2} = i\eta \pm \sqrt{\omega_0^2 - \eta^2}, \tag{16}$$

$$\eta = -\frac{1}{2M}(D + iG), \tag{17}$$

$$\omega_0 = \sqrt{K/M}. \tag{18}$$

The complex frequencies $\bar{\omega}_{1,2} = \omega_{1,2} + i/\tau$ are measured in the experiment. To extract the mass parameter,

DOI: 10.1038/NPHYS3234

we use the sum of the real frequencies:

$$\omega_1 + \omega_2 = \mathrm{Re}(\bar{\omega}_1 + \bar{\omega}_2) \tag{19}$$

$$= \mathrm{Re}(G/M - iD/M) \tag{20}$$

$$= G_z/M. \tag{21}$$

Therefore,

$$M = G/(\omega_1 + \omega_2), \tag{22}$$

where the z-component G of the gyrocoupling vector is obtained from static magnetometry measurements ($M_s = 1.19(3) \times 10^6\,\mathrm{A/m}$), the thickness of the magnetic material ($t_{\mathrm{Co}} = 12.0(1)\,\mathrm{nm}$), and the Skyrmion number ($N = 1$) through

$$G = -4\pi N t_{\mathrm{Co}} M_s/\gamma \tag{23}$$

$$= -1.03(2) \times 10^{-12}\,\mathrm{N/m/s}. \tag{24}$$

We note that the previous equations are based on a definition of frequencies as positive if they correspond to counter-clockwise motion, which is opposite to the definition used in Ref. 6.

Due to the large uncertainties in the frequencies, and in particular of the frequency sum $\Sigma\omega = (\omega_1 + \omega_2) = -0.4(2)\,\mathrm{GHz}$, we cannot determine a meaningful upper limit for the inertia of the bubble: within the error bars, $\Sigma\omega = 0$ and thus $|M| = \infty$ is possible. Also, the sign of $\Sigma\omega$, and thus the sign of M, are not conclusively determined by the data. However, we can derive a highly certain lower limit (confidence 99.999 94 %) for the magnitude of the inertial mass, $|M| > M_{\mathrm{LL}}$. This is possible because M scales inversely with $\Sigma\omega$, and a upper limit for $|\Sigma\omega|$ therefore relates to a lower limit in M. Specifically, this lower limit is derived by $M_{\mathrm{LL}} = |G|/(|\Sigma\omega| + 5\sigma(\Sigma\omega))$, where $\sigma(\Sigma\omega)$ denotes the standard deviation of $\Sigma\omega$. The lower limit for the areal mass density ρ, defined as the mass divided by the area of the domain wall of the bubble (circumference times thickness), is given by $\rho_{\mathrm{LL}} = M_{\mathrm{LL}}/(2\pi t_{\mathrm{Co}}\bar{r})$, where $\bar{r} = 50(10)\,\mathrm{nm}$ is the average radius of the bubble and $t_{\mathrm{Co}} = 12.0(1)\,\mathrm{nm}$ is the total CoB thickness. Therefore, $\rho_{\mathrm{LL}} = 2.0(4) \times 10^{-7}\,\mathrm{kg/m^2}$ (where the error bar represents our measurement uncertainty regarding the size of the bubble).

So far, our method relies on a parabolic approximation for the potential in which the bubble gyrates. In reality, however, the potential can deviate from this approximate case. As detailed in Supplementary

Information V, our method of calculating the mass is robust against perturbations of the potential, provided that the resulting trajectory has a functional form that is consistent with our two-frequency theoretical model.

Finally, we can estimate the dipole moment of the bubble $d = 2.1(4) \times 10^{16}\,\mathrm{Am}^2$ given by the product of the bubble area $A = 7(3) \times 10^{-15}\,\mathrm{m}^2$ with the total CoB thickness t_{Co}, the saturation magnetisation M_s, and a factor 2 to account for the fact that the difference between the magnetisation of the inner and of the outer area of the bubble is $2M_s$. To shift a magnetic dipole in a parabolic potential by the distance r_1, a field gradient of $\partial_r B_z = Kr_1/d$ is required. Our fit values show the presence of a strong gradient $\partial_x B_z^{(r_1)} = 90(50)\,\mu\mathrm{T/nm}$ and $\partial_y B_z^{(r_1)} = -170(100)\,\mu\mathrm{T/nm}$ during the negative part of the pulse. We can write this field gradient as a superposition of the gradient of the applied pulse excitation and an extra gradient. We attribute the presence of this extra gradient to the shrinking of the second bubble during the negative field pulse and to a small additional contribution from the re-alignment of the in-plane components of the spins near the surfaces all over the disk. These in-plane components of the spins near the surfaces are expected in our material due to its relatively small perpendicular anisotropy constant expressed by a quality factor of $Q = 0.86(6)$, which is defined as the perpendicular anisotropy constant K_u normalised to the magnetostatic energy $\mu_0 M_s^2/2$.

---

* These authors contributed equally to this work

† These authors contributed equally to this work; Now at Nano Engineering & Storage Technology Group, School of Computer Science, University of Manchester, Manchester M13 9PL, UK

‡ Now at Department of Physics, Indian Institute of Technology Hyderabad, Ordnance Factory Estate, Yeddumailaram, Andhra Pradesh, 502205, India

1 Skyrme, T. A unified field theory of mesons and baryons. *Nucl. Phys.* **31**, 556–569 (1962).

2 Kiselev, N. S., Bogdanov, A. N., Schäfer, R. & Rößler, U. K. Comment on "Giant Skyrmions Stabilized by Dipole-Dipole Interactions in Thin Ferromagnetic Films". *Phys. Rev. Lett.* **107**, 179701 (2011).

3 Thiele, A. A. Steady-State Motion of Magnetic Domains. *Phys. Rev. Lett* **30**, 230–233 (1973).

4 Papanicolaou, N. & Tomaras, T. N. Dynamics of magnetic vortices. *Nuclear Physics B* **360**, 425–462 (1991).

5 Moutafis, C., Komineas, S. & Bland, J. A. C. Dynamics and switching processes for magnetic bubbles in nanoelements. *Phys. Rev. B* **79**, 224429 (2009).

DOI: 10.1038/NPHYS3234

[6] Makhfudz, I., Krüger, B. & Tchernyshyov, O. Inertia and Chiral Edge Modes of a Skyrmion Magnetic Bubble. *Phys. Rev. Lett.* **109**, 217201 (2012).

[7] Döring, W. Über die Trägheit der Wände zwischen Weißchen Bezirken. *Z. Naturforsch. A* **3**, 373 (1948).

[8] Mochizuki, M. Spin-Wave Modes and Their Intense Excitation Effects in Skyrmion Crystals. *Phys. Rev. Lett.* **108**, 017601 (2012).

[9] Buchanan, K. S. *et al.* Soliton-pair dynamics in patterned ferromagnetic ellipses. *Nat. Phys.* **1, 172–176** (2005).

[10] `http://micromagnum.informatik.uni-hamburg.de`

[11] Thomson, T., Hu, G. & Terris, B. D. Intrinsic Distribution of Magnetic Anisotropy in Thin Films Probed by Patterned Nanostructures. *Phys. Rev. Lett.* **96**, 257204 (2006).

[12] Büttner, F. *et al.* Magnetic states in low-pinning high-anisotropy material nanostructures suitable for dynamic imaging. *Phys. Rev. B* **87**, 134422 (2013).

[13] Malozemoff, A. P. & Slonczewski, J. C. *Magnetic Domain Walls in Bubble Materials* (Academic Press, New York, 1979).

[14] Büttner, F. *et al.* Automatable sample fabrication process for pump-probe X-ray holographic imaging. *Opt. Express* **21**, 30563–30572 (2013).

[15] Barman, A. *et al.* Ultrafast magnetisation dynamics in high perpendicular anisotropy $[Co/Pt]_n$ multilayers. *J Appl. Phys.* **101**, 09D102 (2007)

[16] Fert, A., Cros, V. & Sampaio, J. Skyrmions on the track. *Nat. Nanotech.* **8**, 152–156 (2013).

[17] Sampaio, J. *et al.* Nucleation, stability and current-induced motion of isolated magnetic skyrmions in nanostructures. *Nat. Nanotech.* **8**, 839–844 (2013).

[18] Tchoe, Y. & Han, J. H. Skyrmion generation by current. *Phys. Rev. B* **85**, 174416 (2012).

[19] Lin, S.-Z., Reichhardt, C. & Saxena, A. Manipulation of skyrmions in nanodisks with a current pulse and skyrmion rectifier. *Appl. Phys. Lett.* **102**, 222405 (2013).

[20] Eisebitt, S. *et al.* Lensless imaging of magnetic nanostructures by X-ray spectro-holography. *Nature* **432**, 885–888 (2004).